



MOF-derived hcp-Co nanoparticles encapsulated in ultrathin graphene for carboxylic acids hydrogenation to alcohols

Xiaoqing Gao^{a,b}, Shanhui Zhu^{a,*}, Mei Dong^a, Weibin Fan^{a,*}

^a State Key Laboratory of Coal Conversion, Institute of Coal Chemistry, Chinese Academy of Sciences, Taiyuan 030001, PR China

^b University of Chinese Academy of Sciences, Beijing 100049, PR China



ARTICLE INFO

Article history:

Received 6 March 2021

Revised 1 May 2021

Accepted 7 May 2021

Available online 19 May 2021

Keywords:

Carboxylic acid

Hydrogenation

Co

Facet effect

DFT calculation

ABSTRACT

Highly efficient conversion of carboxylic acids to valuable alcohols is a great challenge for easily corroded non-noble metal catalysts. Here, a series of few-layer graphene encapsulated metastable hexagonal closed-packed (hcp) Co nanoparticles were fabricated by reductive pyrolysis of metal-organic framework precursor. The sample pyrolyzed at 400 °C (hcp-Co@G400) presented outstanding performance and stability for converting a variety of functional carboxylic acids and its turnover frequency was one magnitude higher than that of conventional fcc-centered cubic (fcc) Co catalysts. In situ DRIFTS spectroscopy of model reaction acetic acid hydrogenation and DFT calculation results confirm that carboxylic acid initially undergoes dehydroxylation to RCH₂CO* followed by consecutive hydrogenation to RCH₂CH₂OH through RCH₂COH*. Acetic acid prefers to vertically adsorb at hcp-Co (002) facet with a much lower adsorption energy than parallel adsorption at fcc-Co (111) surface, which plays a key role in decreasing the activation barrier of the rate-determining step of acetic acid dehydroxylation.

© 2021 Elsevier Inc. All rights reserved.

1. Introduction

With the rapid development of biomass conversion in recent years, numerous bio-based carboxylic acids, such as levulinic acid (LA), succinic acid, lactic acid and itaconic acid have been emerged as versatile platform chemicals [1,2]. Reduction of carboxylic acids to alcohols, particularly for diols, is industrially important because the generated alcohols are intermediates for a variety of polyesters, pharmaceuticals, agrochemicals and fine chemicals [3,4], e.g. 1,4-butanediol is an important commodity chemical to produce valuable polymers over 2.5 million tons annually, and it is currently manufactured through the feedstocks from fossil resources [5,6]. Thus, the development of a green and cost-effective approach is highly desirable to synthesize alcohols via the reduction of biomass-derived carboxylic acid.

Currently, the production of alcohols from carboxylic acids has been performed using stoichiometric quantities of strong reducing agents including toxic metal hydrides or silanes [7], which inevitably results in serious environmental issues. In recent years, much progress has been made in the use of homogenous Ru and Ir or heterogeneous Ru, Rh, Pd and Pt-based catalysts for carboxylic acids hydrogenation [8–12]. Nevertheless, it is still a grand

challenge to effectively perform hydrogenation of carboxylic acids by cheaper, more abundant and less toxic base metals (such as Co, Fe, Ni and Cu). Compared to ketones and esters, carboxylic acids are difficult to reduce by H₂ owing to the low electrophilicity of carbonyl carbon [7]. Additionally, the strong acidity of carboxylic acids can seriously corrode and damage base metals, leading to detrimental catalyst deactivation. Very recently, Bruin et al. [13] have reported the first earth-abundant homogenous Co(BF₄)₂·6H₂O catalyst capable of hydrogenating a series of functionalized carboxylic acids to alcohols with superior activity. Encouragingly, it is anticipated to design a highly active heterogeneous Co-based catalyst to overcome strong acidity and inert carboxyl groups.

Metal-organic frameworks (MOFs) are usually consisted of base metal and organic ligands with porous and tuneable structure. Recently, MOFs have emerged as promising self-sacrificing templates for synthesizing some metals nanoparticles (NPs), oxides, carbon or their composites via simple pyrolysis [14–20], enabling to tailor their compositions, shapes and phase structures by tuning MOFs sources, preparation conditions or postsynthetic modifications. For example, Beller et al. [18] have fabricated Co and Co₃O₄ composite NPs encapsulated by graphitic shell via the pyrolysis of cobalt-diamine-dicarboxylic acid MOFs under inert Ar atmosphere, which are broadly effective in reductive amination. Additionally, more complex MOFs-related Co-based catalysts have been created, such as Co-CoO@N-doped porous carbon [21], CoS₂

* Corresponding authors.

E-mail addresses: zhushanhui@sxicc.ac.cn (S. Zhu), fanwb@sxicc.ac.cn (W. Fan).

nanobubble hollow prisms [22], or $\text{Co}_3\text{O}_4@\text{NiCo}_2\text{O}_4$ double-shelled nanocages [23], which may offer us potential opportunities to fabricate highly stable Co NPs to tolerate carboxylic acid.

The catalytic performances of metal NPs are highly dependent on their crystal structure, so-called structure sensitivity [24,25]. Metal Co possesses two crystallographic structures, i.e. metastable hexagonal closed-packed (hcp) phase and thermodynamically stable face-centered cubic (fcc) phase. The hcp and fcc Co have different bulk symmetries and structure, and thus lead to expose distinct facets, which directly influences catalytic performance. Using conventional approaches such as impregnation, precipitation or sol-gel, the synthesized Co-based catalysts are composed of fcc Co or their mixed phases after the reduction of their precursors Co_3O_4 , CoO or spinel by H_2 [26,27]. Although many researchers argue that hcp Co is more active than fcc phase in their mixed catalysts, such as well-known Fischer-Tropsch synthesis, the intrinsic active phase is still in great debate for decades owing to the significant challenge for the synthesis of single hcp Co phase [25,28,29].

In this context, we made a try to pyrolyze MOF precursor of $\text{Co}_3[\text{Co}(\text{CN})_6]_2$ in reductive atmosphere. Unexpectedly, the single phase hcp-Co NPs were obtained and encapsulated by few-layer graphene. The as-prepared hcp-Co exhibited enhanced performance in one magnitude in comparison to fcc-Co in carboxylic acid hydrogenation. Combined with in situ diffuse reflection Fourier transform infrared spectra (DRIFTS) model reaction of acetic acid hydrogenation and density functional theory (DFT) calculation results, the reaction mechanism of carboxylic acid hydrogenation have been disclosed, in which dehydroxylation is identified as a key step in the formation of alcohol.

2. Experimental section

2.1. Catalyst preparation

0.04 mmol $\text{K}_3[\text{Co}(\text{CN})_6]$ (J&K Scientific Ltd.) and 0.3 g polyvinylpyrrolidone (PVP, Aladdin) were first dispersed in 10 mL water under vigorous stirring. Then, 10 mL 0.0075 mol/L $\text{Co}(\text{NO}_3)_2 \cdot 6\text{H}_2\text{O}$ (Aladdin) aqueous solution was dropwisely added at room temperature. After stirring for 10 min, the mixed solution was transferred into Teflon-lined stainless steel autoclave and kept at room temperature for 24 h. The solid was collected by centrifugation, washed with water and ethanol, and dried at 80 °C overnight. Finally, these collected solids were pyrolyzed at 300, 400, 500, 600 or 700 °C in 10 vol% H_2/Ar gas for 6 h, and passivated in 1 vol% O_2/Ar gas at room temperature for 2 h. The as-prepared catalysts were designated as hcp-Co@GT, where T refers to annealing temperature.

G400 was synthesized by the treatment of hcp-Co@G400 with 98% sulfur acid at 180 °C for 24 h, followed by centrifugation, washing and drying at 80 °C overnight.

The fcc-Co@G400 catalyst was prepared as follows: certain amounts of $\text{Co}(\text{NO}_3)_2 \cdot 6\text{H}_2\text{O}$ (Sinopharm Chemical Reagent Co., Ltd., China (SCRC)), 0.3 g PVP, and 0.8 g G400 were successively added into 10 mL water under vigorous stirring for 1 h. The collected solid was separated by centrifugation, dried and annealed in 10 vol% H_2/Ar at 400 °C for 6 h. The Cu@G400, Ni@G400 or Fe@G400 catalysts were prepared with the same method as above.

2.2. Catalyst characterization

N_2 adsorption-desorption isotherms were recorded at –196 °C on a Micromeritics TriStar 3000 instrument. Before the measurements, all the catalysts were pretreated under vacuum at 250 °C for 8 h under high vacuum condition.

The Co contents were measured by inductively coupled plasma atomic emission spectroscopy (ICP-AES) apparatus (Optima 2100DV, PerkinElmer). Prior to the measurements, the samples were heated at 700 °C for 2 h in air, and treated with hydrochloric acid at 120 °C for 12 h.

Powder X-ray diffraction (XRD) patterns and in situ XRD were conducted on a D8/max-X-ray diffractometer (Bruker, Germany) operating with Cu K α radiation. In situ XRD patterns of $\text{Co}_3[\text{Co}(\text{CN})_6]_2$ were recorded at different temperature and time with a heating rate of 5 °C/min in flowing 10 vol% H_2/Ar gas.

In situ diffuse reflectance ultraviolet-visible (UV-vis) spectra were performed at Agilent Cary 5000 UV-Vis-NIR spectrophotometer equipped with a poly(tetrafluoroethylene) integrating sphere. During the measurements, $\text{Co}_3[\text{Co}(\text{CN})_6]_2$ was heated to 400 °C with a heating rate of 5 °C/min and kept at this temperature for 6 h in flowing 10 vol% H_2/Ar gas.

Raman spectroscopy was carried out on a Renishaw-UV-vis Raman System 1000 instrument using a CCD detector at room temperature. The 532 nm of Nd:YAG laser was employed as the excitation source with a power of 30 MW.

Transmission electron microscopy (TEM) and high resolution TEM (HRTEM) measurements were taken on a field-emission transmission electron microscopy (FETEM, JEM-2011F) operating at 200 kV voltages.

X-ray photoelectron spectroscopy (XPS) was measured on a VG MiltiLab 2000 spectrometer with Mg K α radiation and a multi-channel detector. The binding energies were calibrated using the C1s peak at 284.5 eV. The reduced catalyst is obtained by in situ treating the passivated sample at 300 °C for 2 h in a 10 vol% H_2/Ar flow.

Co K-edge X-ray absorption spectroscopy (XAS) was performed in fluorescence mode at the beam line of Beijing Synchrotron Radiation Facility (BSRF), Institute of High Energy Physics (IHEP), Chinese Academy of Science (CAS). XAS spectra was processed in Athena XAS version 0.8.056 software, in which background subtraction and normalization were fitted linear polynomials to the pre-edge and post-edge regions of absorption spectra, respectively. The E_0 value was calculated based on the maximum value in the first derivative of the edge region.

In situ DRIFTS was carried out in a FTIR spectrophotometer (Nicolet Is10) operating with a SMART collector and an MCT detector cooled in liquid N_2 . 40 mg catalyst was initially pretreated at 300 °C for 2 h in H_2/Ar gas (20 mL/min), and cooled down to room temperature in Ar gas. Subsequently, acetic acid was introduced into the catalyst surface and gradually reached in saturated state, which was monitored by DRIFTS spectra. With increasing temperature to 220 °C, the adsorbed acetic acid began to desorb from the catalyst. Once the DRIFTS spectra of adsorbed acetic acid kept stable, H_2 (20 mL/min) was introduced into the system and the DRIFTS spectra were simultaneously collected.

2.3. Catalytic tests

Before the reaction test, the catalyst was activated in 10 vol% H_2/Ar at 20 mL/min in 300 °C for 2 h. Unless otherwise specified, 1 mmol substrate, 0.05 g catalyst and 5 mL H_2O were charged into a stainless steel autoclave (NS-10316L, Anhui Kemi Machinery Technology Co., Ltd.). The reactor was sequentially purged with H_2 for 5 times, pressured to 5.0 MPa H_2 , heated into 220 °C, and kept at this temperature for 24 h. After the reaction, the reaction system was quickly cooled to room temperature in an ice-water bath. After separation, the liquid products were analyzed by gas chromatography (Shimadzu GC-2010) with a flame ionization detector. 1,2-butanediol was used as an internal standard for the formation of diol, while 1-butanol was applied in the case of monohydric alcohol. The insoluble reactants and products in water were

extracted by ethyl acetate, and analyzed with ethyl benzoate as internal standard. Diethyl ether was used as extract in the conversion of stearic acid and palmitic acid. The gas products were analyzed by Agilent 7890A gas chromatograph equipped with a TCD detector. All the products were identified by a Shimadzu GCMS-QP2010 gas chromatogram–mass spectrometer (GC-MS) and NMR spectroscopy (Bruker AV-III 400 MHz NMR spectrometer).

The turnover frequency (TOF) in the conversion of acetic acid was calculated based on surface Co atoms at low conversion. The surface Co atoms were estimated on total Co atoms and Co dispersion. According to previous report [30], Co dispersion (D) can be calculated by the equation $D = 96/d$, in which d refers to Co mean particle size in nm from TEM counting.

$$\text{TOF} = \frac{\text{Mole number of converted acetic acid}}{\text{Number of surface Co atoms} \times \text{reaction time}}$$

In the catalytic reusability tests, the used hcp-Co@G400 catalyst was magnetically separated from the reaction mixture. The collected catalyst was directly reused for the next run.

2.4. DFT calculation

Periodic DFT calculations were performed in Vienna *ab initio* simulation package (VASP) with projector-augmented wave (PAW) method [31]. Exchange and correlation energies were treated with spin-polarized generalized gradient approximation and Perdew, Burke, and Ernzerhof (PBE) functional [32]. A plane wave energy cutoff was set as 450 eV, and a $4 \times 4 \times 1$ Monkhorst-Pack k -points were used.

The hcp Co (002) and fcc Co (111) surfaces were modeled by a four-layer slab with 3×3 unit cell. A 15 Å vacuum layer was set between the slabs to avoid interlayer interactions along z -direction. The top two layers of Co atoms and adsorbates were fully relaxed, while the bottom two layers were fixed during the calculation. The adsorption energy (E_{ads}) are defined as the equation $E_{\text{ads}} = E_{\text{ads/slab}} - E_{\text{gas}} - E_{\text{slab}}$, in which $E_{\text{ads/slab}}$, E_{ads} and E_{slab} are the energies of the adsorbate with slab, adsorbate in the gas phase, and the clean slab, respectively.

The transition states calculations were implemented by climbing image nudge elastic band (CI-NEB) method [33]. All the transition states were validated by vibrational frequency analysis. The activation energy barrier (E_a) and reaction energy (E_r) were determined by $E_a = E_{\text{TS}} - E_{\text{IS}}$ and $E_r = E_{\text{FS}} - E_{\text{IS}}$, wherein E_{IS} , E_{TS} , and E_{FS} are the energies of the initial state (IS), transition state (TS) and final state (FS), respectively.

3. Results and discussion

3.1. Fabrication of hcp-Co@G and structure characterization

Prussian blue analogues (PBA) are one of the most extensively explored MOFs for their uniform sizes, special thermal properties and unique reactivity [34,35]. A series of core-shell structure catalysts were prepared by pyrolyzing PBA-structured $\text{Co}_3[\text{Co}(\text{CN})_6]_2$ NPs at different temperature in 10% H_2/Ar flow. As illustrated in Fig. 1, the TEM and HRTEM images show that all the uniform Co NPs in hcp-Co@G400 are well encapsulated by ultrathin graphene shell. Considering its ultrahigh Co content up to 63.1% (Table 1), the average Co particle size of 8.8 nm indicates its formation of rather homogenous Co NPs. The formation of metastable hcp-Co can be identified by its (111) lattice fringe of 0.202 nm [26], and no fcc Co is detected.

Statistical analysis of more than 300 core-shell nanocomposites confirms that the number of graphene shell is only consisted of 2–5 layers. Careful observation in HRTEM images show that the gra-

phene layers outside Co NPs are not totally closed, and some cracks in 0.2–0.8 nm can be found. The annealed samples were fiercely oxidized once it exposed to air, implying that O_2 molecules can freely pass through graphene layers via cracks to react with hcp-Co species. Notably, these cracks play a decisive role in exposing active Co facets for catalytic reaction.

For other samples annealing at 300, 500, 600 and 700 °C (Figs. S1–S4), all the hcp-Co NPs are well covered by graphene shell, despite with many cracks. The increased pyrolysis temperature improves Co particle size, graphene layers and graphitization degree, but correspondingly declines graphene defects and cracks. For Co@G300, the presence of both hcp-Co and $\text{Co}_3[\text{Co}(\text{CN})_6]_2$ species in XRD patterns indicates that $\text{Co}_3[\text{Co}(\text{CN})_6]_2$ is not completely decomposed at 300 °C, as supported by its low Co content but high N content (Table 1). The BET surface area of hcp-Co@G300 reaches 332.4 m^2/g and is much higher than other high temperature samples, also suggesting that it contains some remaining $\text{Co}_3[\text{Co}(\text{CN})_6]_2$ species.

As displayed in Fig. 2a, the diffraction reflections at 17.4°, 24.7°, 35.2°, 39.5° and 51.4° are ascribed to $\text{Co}_3[\text{Co}(\text{CN})_6]_2$ over hcp-Co@G300 [34]. The reflections at 41.4°, 44.5° and 47.4° are assigned to (010), (002) and (011) planes of hcp-Co phase [26]. Both $\text{Co}_3[\text{Co}(\text{CN})_6]_2$ and hcp-Co species are co-existed in hcp-Co@G300, suggesting the incomplete decomposition of $\text{Co}_3[\text{Co}(\text{CN})_6]_2$. The diffraction peaks of hcp-Co gradually increase in intensity with increasing annealing temperature, indicating a steady growth of Co particle size. The increase of Co particle size is also supported by TEM statistical analysis. Additionally, TEM and XRD results show that (002) plane is the most exposed facet in all the hcp-Co@G catalysts.

The Raman spectra of all the samples are illustrated in Fig. 2b. The well-resolved two bands at 1344 and 1574 cm^{-1} are assigned to D and G bands, respectively [15,21]. The D band is associated with defects or disordered carbon, while G band refers to sp^2 -hybridized graphitic carbon [15]. The hcp-Co@G300 catalyst show very low intensity of D and G bands owing to the preservation of substantial $\text{Co}_3[\text{Co}(\text{CN})_6]_2$. The relative intensity of I_G/I_D is indicative of graphitization degree. For other samples, the I_G/I_D ratio increases with increasing annealing temperature and indicates an improved graphitization degree, coincident with the enhanced graphene layer number [21].

Unexpectedly, pure hcp Co NPs are successfully fabricated and remain stable even at high temperature up to 700 °C, which has never been reported. The hcp Co is only stable below the allotropic transformation temperature (420–450 °C), whereas the fcc structure is thermodynamically stable above this temperature [36]. Previous studies [28,29] have shown that the control synthesis of pure hcp-Co is a great challenge when the preparation process needs high temperature thermal treatment. Thus, the formation mechanism of graphene encapsulated hcp-Co species was necessarily probed by in situ UV–vis spectra and in situ XRD (Fig. 3a,b and Fig. S5). In comparison with XRD, UV–vis spectroscopy is more sensitive to detect surface or minor metal cation species. Fig. 3a in UV–vis spectra show that the as-prepared $\text{Co}_3[\text{Co}(\text{CN})_6]_2$ displays many peaks at 250, 320, 528, 600, 638 and 690 nm, which are associated with Co^{2+} and Co^{3+} . When the annealing temperature enhanced from 30 °C to 100 °C, the presence of very strong adsorption band at 587 nm is ascribed to the isolated mononuclear octahedral Co^{2+} [37], originating from the decomposition of $\text{Co}_3[\text{Co}(\text{CN})_6]_2$. A moderate decline in characteristic peak intensity of $\text{Co}_3[\text{Co}(\text{CN})_6]_2$ is also observed in in situ XRD pattern (Fig. 3b) at 100 °C. The characteristic band of isolated Co^{2+} is still detected up to 400 °C at UV–vis spectra. Simultaneously, new XRD diffraction reflections at 41.3°, 42.6° and 45.2° appear, which are assigned to Co_2C crystalline [38]. With increasing annealing time (Fig. S5) or temperature (Fig. 2b), the Co_2C characteristic peaks disappear both in UV–vis spectra and XRD patterns. Since

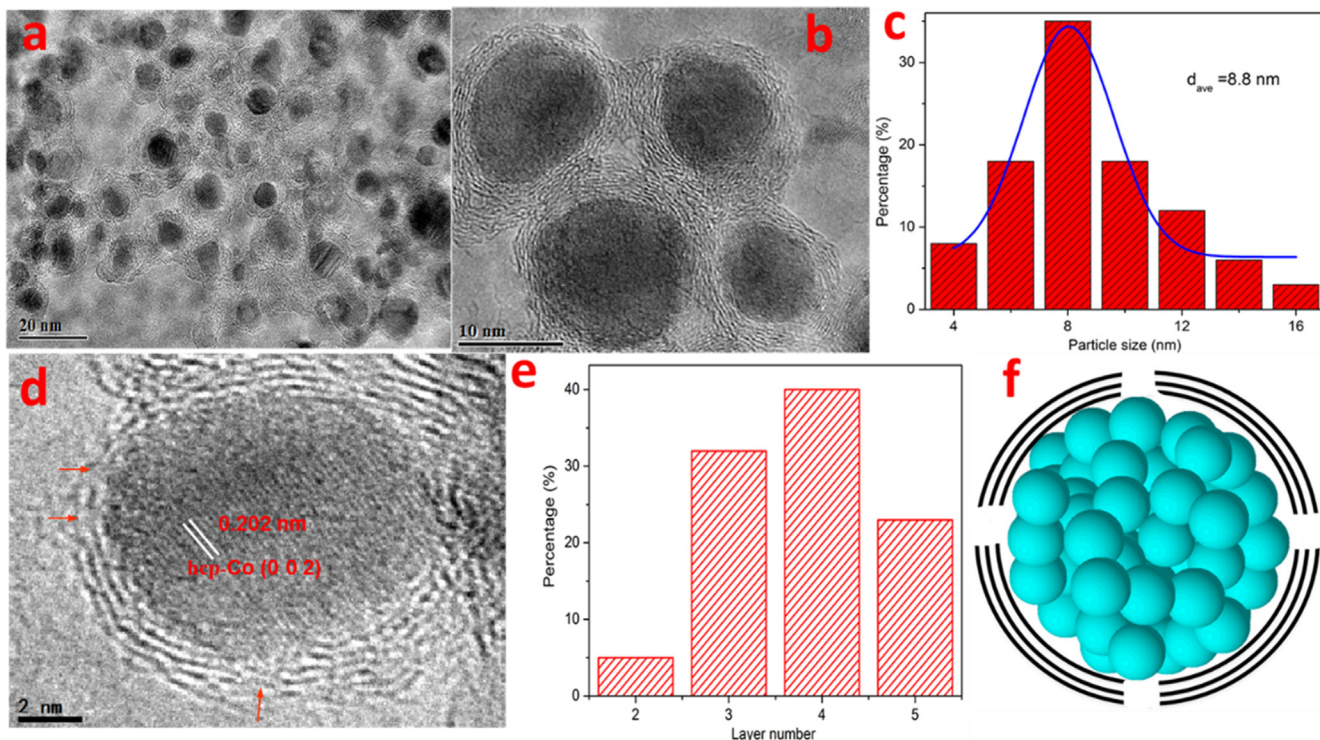


Fig. 1. (a, b, d) TEM and HRTEM images of hcp-Co@G400; (c) hcp-Co NPs size distribution; (e) statistical analysis of graphene layer number distribution in the graphene shell; (f) schematic illustration of hcp-Co@G400 structure.

Table 1
Textural and physicochemical properties for various catalysts.

Catalyst	BET surface area (m ² /g)	Pore volume (cm ³ /g)	Pore size (nm)	Co content (wt. %) ^a	Co particle size (nm) ^b	Dispersion (%)	N content (at.%) ^c
hcp-Co@G300	332.4	0.288	15.4	29.8	8.0	12.0	17.6
hcp-Co@G400	88.4	0.385	21.4	63.1	8.8	10.9	2.9
hcp-Co@G500	56.1	0.297	25.3	63.6	10.5	9.1	2.2
hcp-Co@G600	50.2	0.284	25.1	64.0	12.6	7.6	2.1
hcp-Co@G700	50.3	0.289	24.4	64.3	13.8	7.0	2.0
20fcc-Co@G400	75.1	0.367	22.8	19.1	7.0	13.7	3.9
60fcc-Co@G400	48.9	0.264	24.0	62.5	12.4	7.7	1.7

^a Tested by ICP.

^b Determined by TEM.

^c Obtained by EA.

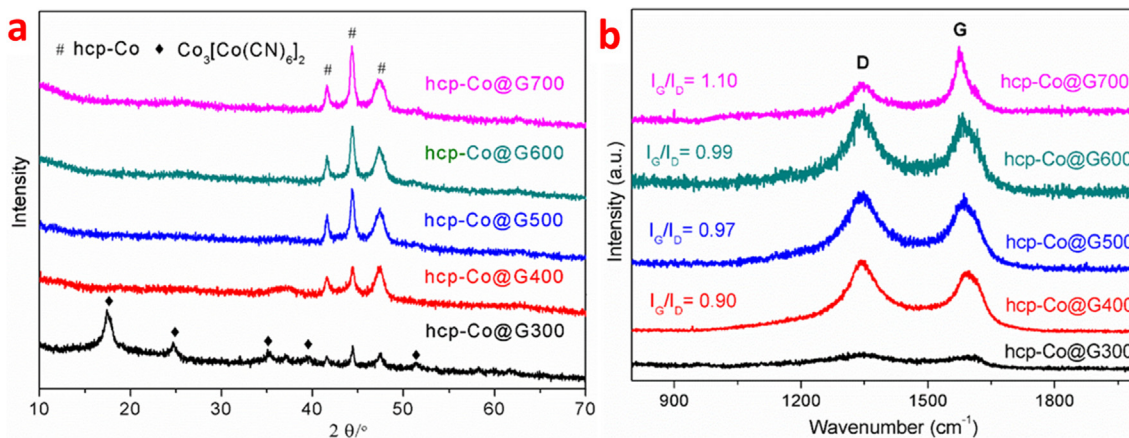


Fig. 2. (a) XRD patterns and (b) Raman spectra of hcp-Co@GT catalysts annealed at various temperatures.

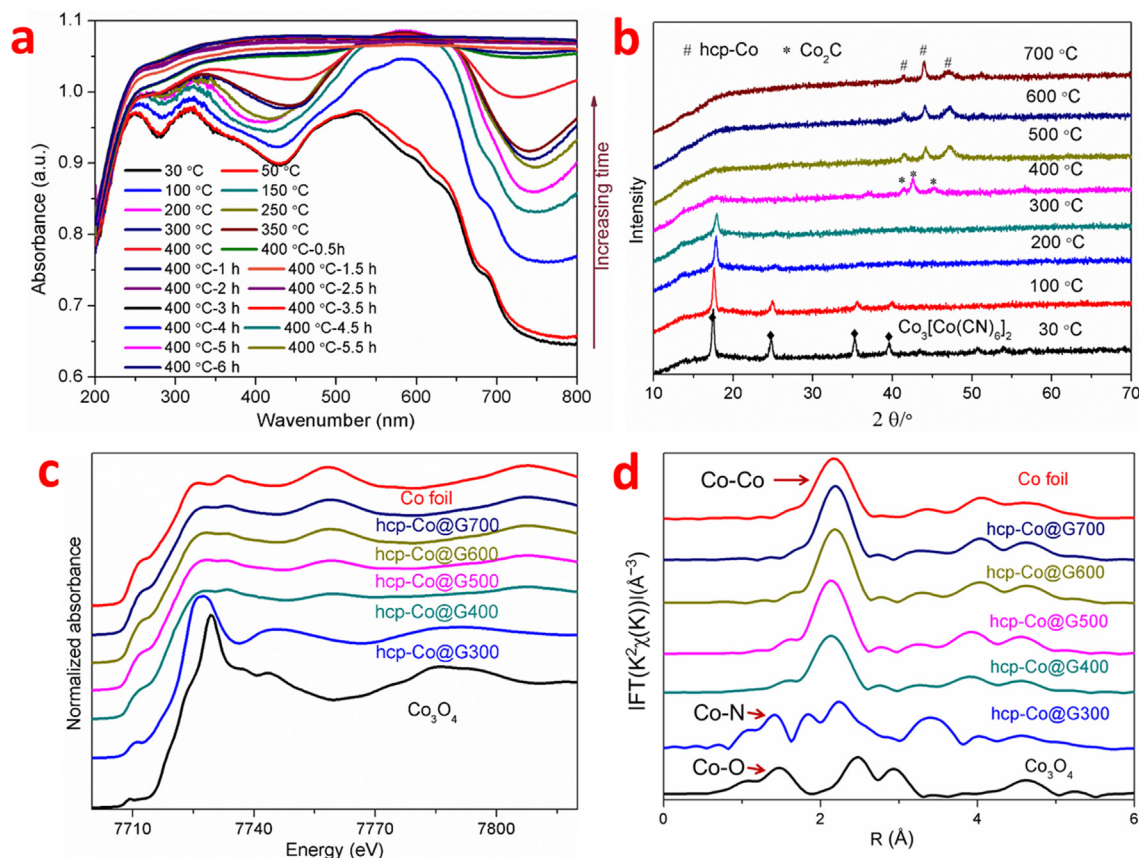


Fig. 3. (a) In situ UV-vis and (b) in situ XRD patterns for annealing $\text{Co}_3[\text{Co}(\text{CN})_6]_2$ in H_2/Ar gas with a heating rate of $5^\circ\text{C}/\text{min}$. (c) Co K-edge XANES and (d) Fourier transformed EXAFS spectra of hcp-Co@GT catalysts, Co foil and Co_3O_4 .

then, no any obvious peaks are detected by UV-vis spectra, reflecting that there is no oxidized Co species. Indeed, only reduced hcp-Co species diffraction reflections are detected by XRD. The above results indicate that the Co_2C from $\text{Co}_3[\text{Co}(\text{CN})_6]_2$ decomposition is rapidly reduced into metastable hcp-Co. Metallic hcp-Co NPs can catalytically promote the growth of graphene around their edges, and are further confined in graphene shell. The core-shell structure can inhibit the occurrence of allotropic transformation of hcp-Co into fcc-Co below 700°C .

XPS spectroscopy (Fig. S6) analysis, X-ray absorption near-edge structure (XANES, Fig. 3c), and extended X-ray absorption fine structure (EXAFS, Fig. 3d) were employed to determine the chemical states and coordination of the Co atoms in hcp-Co@G catalysts. As displayed in Fig. S6, hcp-Co@G400 and other high temperature samples present two peaks at around 778.5 and 793.5 eV, which are assigned to $2p_{3/2}$ and $2p_{1/2}$ spectra of metallic Co^0 [21], respectively. The spent hcp-Co@G400 still displayed only Co^0 characteristic peaks, indicating that Co^0 active sites kept stable during the reaction. For hcp-Co@G300, another two broad peaks at 782.1 and 797.3 eV are associated with $\text{Co}^{2+/3+}$ of $\text{Co}_3[\text{Co}(\text{CN})_6]_2$. Except for hcp-Co@G300, all the hcp-Co@G catalysts show similar XANES spectra as Co foil (Fig. 3c), suggesting that Co species are only existed as metal state. The EXAFS results show that only Co-Co bonds were detected for the above samples, consistent with XPS results for the detection of Co^0 . In the case of hcp-Co@G300, its pre-edge peak is located at 7710.5 eV, lower than that of Co foil (7711.4 eV) and higher than that of Co_3O_4 (7709.0 eV). This suggests that it contains different types of Co species. The preservation of Co-N bond is verified by its bond length of 1.42 Å over hcp-Co@G300 in EXAFS [39]. Combined with XANES, EXAFS, and XRD

results, it can be deduced that both undecomposed $\text{Co}_3[\text{Co}(\text{CN})_6]_2$ and hcp-Co are present in the hcp-Co@G300.

3.2. Catalytic performance for carboxylic acid hydrogenation

LA and acetic acid are two of the most important biomass-related carboxylic acids [40,41]. Therefore, these two acids are selected as model compounds for hydrogenation at 220°C and 5.0 MPa H_2 . According to the reaction pathway of LA hydrogenation (Scheme S1), the reduction of carbonyl and carboxylic group is competitive, and the product distribution is highly dependent on catalyst composition. As shown in Fig. 4a and Table S1, all the hcp-Co@G catalysts exhibited complete LA conversion but with various 1,4-pentanediol (1,4-PDO) yields, because carbonyl group are much more easily reduced than carboxylic group in LA. Hcp-Co@G300 gave 29.9% yield of target product 1,4-PDO along with a variety of by-products, including 19.1% γ -valerolactone (GVL), 11.7% 2-methyl tetrahydrofuran (MTHF), and 3.1% 1-pentanol. The poor 1,4-PDO yield of hcp-Co@G300 is primarily ascribed to its low hcp-Co content, originating from the incomplete decomposition of $\text{Co}_3[\text{Co}(\text{CN})_6]_2$. Of all the examined catalysts, hcp-Co@G400 exhibited dramatic enhancement in 1,4-PDO yield, reaching 89.5%. However, an increase of annealing temperature gradually declined the yield of 1,4-PDO as a result of increased GVL yield. Because these catalysts cannot effectively reduce carboxylic into hydroxyl group, the intermediate product 4-hydroxyl pentanoic acid (HPA) cannot be converted into 1,4-PDO but undergoes lactonization to form GVL.

Additionally, we used sulfuric acid to completely etch Co species from hcp-Co@G400 in order to prepare G400 support.

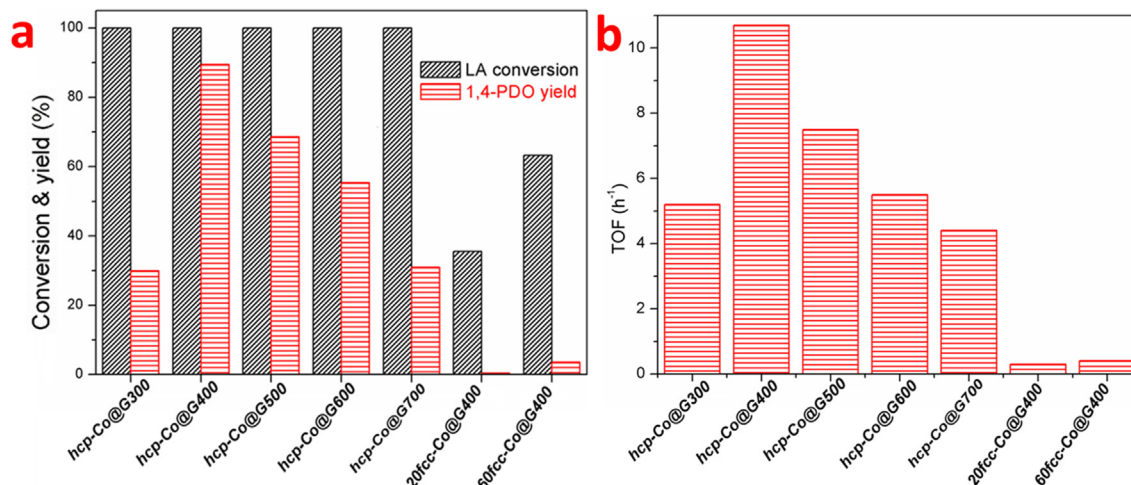


Fig. 4. (a) Catalytic performance of LA hydrogenation over various catalysts. Reaction conditions: 1 mmol LA, 0.05 g catalyst, 220 °C, 5 MPa, 24 h. (b) TOF value of acetic acid hydrogenation over various catalysts.

ICP-AES result confirmed that the hcp-Co species had been totally removed. The G400 support was nearly inactive for LA conversion (Table S1). Subsequently, 20fcc-Co@G400 and 60fcc-Co@G400 catalysts were prepared from $\text{Co}(\text{NO}_3)_2 \cdot 6\text{H}_2\text{O}$ with similar methods as hcp-Co@G400. These two catalysts only contain fcc-Co crystalline phase, as confirmed by TEM (Figs. S7–S8) and XRD (Fig. S9) measurements. Both of them exhibited very poor performance for LA hydrogenation, and their yields of 1,4-PDO were only 0.4% and 3.6%, respectively. These evaluation results unambiguously confirm the superior activity of hcp-Co to fcc-Co. Additionally, other base metal catalysts, such as Cu, Ni and Fe, also showed very poor yields of 1,4-PDO.

To better reflect the reduction ability of carboxylic group for these catalysts, the model reaction of acetic acid hydrogenation was performed to estimate their intrinsic turnover frequency (TOF, Fig. 4b and Table S2). All the catalysts obtained high ethanol selectivity (greater than 93%) along with small amounts of by-product ethane. The activity trend was similar to their performance in LA hydrogenation. The TOF value of hcp-Co@G400 reached 10.7 h^{-1} , higher than those catalysts annealed at other temperatures. The remaining $\text{Co}_3[\text{Co}(\text{CN})_6]_2$ species in hcp-Co@G300 cannot contribute to TOF, and decreased its value to 5.2 h^{-1} . For the catalysts annealed at temperature higher than 400 °C, the increased graphene layer numbers greatly inhibited the adsorption of acetic acid (Fig. S10), leading to low reaction performance. As confirmed by DRIFTS of acetic acid adsorption in Fig. S10, the peak area of acetic acid adsorption (at 1726, 1468 and 1291 cm^{-1}) of hcp-Co@G400 was much higher than other samples. Both 20fcc-Co@G400 and 60fcc-Co@G400 gave very limited TOF in acetic acid hydrogenation, only 0.3 h^{-1} and 0.4 h^{-1} , respectively. Their TOF values were even one magnitude lower than that of hcp-Co@G counterparts. The particle size effects on the TOF can be excluded since both Co particles are centered at $10 \sim 13 \text{ nm}$ for 60fcc-Co@G400 and hcp-Co@G500, 600 and 700 catalysts with similar Co content. Thus, the huge difference in reactivity is strongly related to Co crystalline phase.

The time course of LA hydrogenation over hcp-Co@G400 is displayed in Fig. S11. LA conversion sharply increased to 100% in 4 h. With increasing reaction time to 24 h, the yield of 1,4-PDO gradually improved at the expense of GVL. The reaction trend confirms that LA preferentially undergoes the hydrogenation of carbonyl group in comparison to carboxylic group. 1,4-PDO yield reached the maximal value of 89.5% at 24 h. The reaction stability is a very important criterion to evaluate strong acidic carboxylic acid

hydrogenation, particularly for non-precious metal catalysts. As displayed in Fig. 5a, no any decrease in LA conversion and 1,4-PDO yield was observed over hcp-Co@G400 in the reusability tests. The graphene encapsulated hcp-Co nanostructures were still well preserved after six reaction cycle tests, as confirmed by TEM images (Fig. S12). Moreover, ICP-AES test verified that only 1.1% Co content was leached, suggesting that the graphene shell can protect Co from leaching and corrosion caused by LA. In a control experiment, the supported 60fcc-Co@G400 (Fig. 5b) without graphene overcoat exhibited irreversible deactivation due to substantial Co leaching (18.7%).

Considering the excellent performance in LA and acetic acid hydrogenation over hcp-Co@G400, we investigated its substrate scope for other typical carboxylic acid, particularly for biomass-derived acids (Table 2). More than 90% yields of alcohols were obtained in the conversion of short-chain monoaliphatic acids and challenging long-chain acids, such as palmitic and stearic acid. Diols are of special interest because of their vital role in manufacturing polyesters [5,10], particularly using the biomass-related carboxylic acids as feeds. We were pleased to find that these typical bio-based carboxylic acids, including LA, lactic, succinic, adipic, itaconic acids, were smoothly converted into desired diols with good to excellent yields. Moreover, many aromatic acids, such as furoic, benzoic and functionalized benzoic acids, can also be reduced efficiently in 75.6–94.6% yields. Notably, the aromatic rings, $-\text{NO}_2$, and aromatic ether were initially reduced, suggesting that the reduction of carboxylic group is very challenging relative to other reductive groups. However, there are still some limitations for this catalytic system. The selective hydrogenation of carboxylic moieties over other functional groups is very important for the synthesis of some special chemicals [9,42]. The aromatic $\text{C}=\text{C}$ bonds in furan or benzene rings are preferentially reduced over hcp-Co@G400, which results in total disappearance of aromaticity in the target alcohol.

3.3. Reaction mechanism for carboxylic acid hydrogenation

So far, the reaction mechanism of carboxylic acid (RCOOH) hydrogenation still remains great debate on the initial dehydrogenation to form RCOO^* and then deoxygenation to RCO^* or direct dehydroxylation to generate RCO^* [13,43,44]. Another key question is whether aldehyde (RCHO) is involved by RCO^* hydrogenation [45,46]. To explore possible reaction mechanism, we initially performed the reaction kinetics of acetic acid hydrogenation over

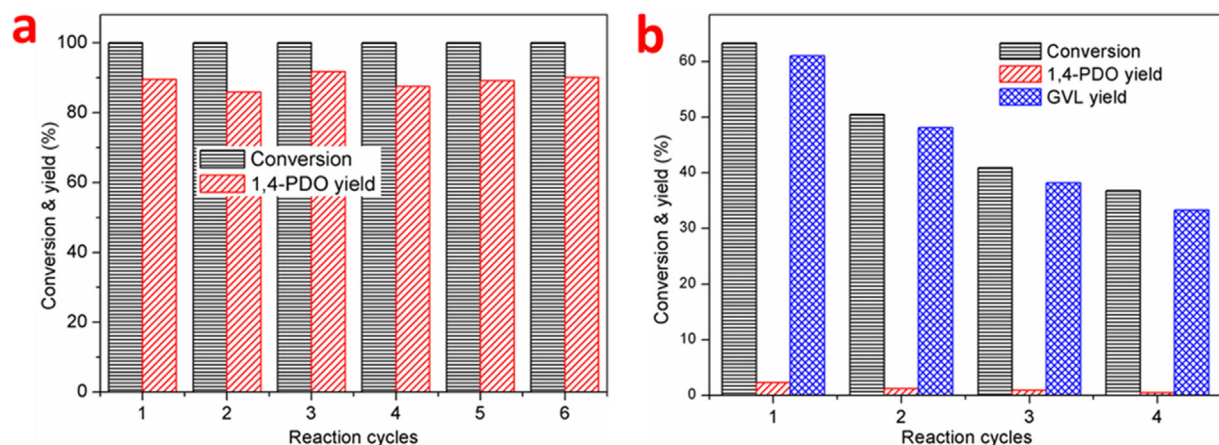


Fig. 5. Reusability tests for LA hydrogenation over (a) hcp-Co@G400 and (b) 60fcc-Co@G400. Reaction conditions: 1 mmol LA, 0.05 g catalyst, 220 °C, 5 MPa, 24 h.

Table 2
Reaction results of various functional carboxylic acids hydrogenation to alcohols over hcp-Co@G400.^a

Substrate	Alcohol product	Time (h)	Con. (%)	Yield (%)		Substrate	Alcohol product	Time (h)	Con. (%)	Yield (%)	
				Alcohol	Alkane					Alcohol	Alkane
		2	100	93.4	5.0			24	100	81.7	1.1
		2	100	95.1	3.2			24	100	94.4	0.7
		2	100	98.4	0.5			24	100	73.2	1.2
		2	100	99.5	0.2			24	100	81.9	8.7
		2	100	96.8	2.7			12	100	94.6	2.3
		24	99.8	90.8	3.4			24	100	89.4	8.9
		24	98.9	92.3	3.0			24	100	86.8	9.4
		24	100	89.5	2.8			24	100	75.6	4.2
		2	100	91.4	0.9			24	100	90.1	3.6

^a Reaction conditions: 1 mmol substrate, 0.05 g catalyst, 220 °C, 5 MPa H₂, 2 or 24 h. Conversion and yield were determined by GC with internal standard method. 1,2-butanediol and 1-butanol were generally used as internal standards for the formation of diol and monohydric alcohol, respectively. The detailed analysis procedure was described in Section 2.3.

hcp-Co@G400 catalyst. As illustrated in Fig. 6a, the reaction order with respect to H₂ pressure was calculated to be 0.58, indicating that the reaction rate was moderately affected by H₂ pressure. As the dissociation of H₂ is very fast on Co surface, the further reaction of dissociated H* may require high reaction energy barrier. The reaction order with respect to acetic acid concentration (Fig. 6b) was estimated to be 0.08, suggesting that acetic acid is strongly adsorbed on hcp-Co surface, in well line with DFT calculation results (see below).

To deeply understand the huge difference in reactivity of hcp-Co and fcc-Co, the surface reaction process was monitored by in situ DRIFTS of acetic acid hydrogenation. Notably, acetic acid

cannot chemically adsorbed on support alone (Fig. S10). As displayed in Fig. 7a, three typical peaks centered at 1726, 1468 and 1291 cm⁻¹ are assigned to C=O stretching, CH₃ bending, C–O stretching vibrations of adsorbed acetic acid over hcp-Co@G400 [47,48], respectively. After introduction of flowing H₂ at 220 °C, the peak intensity of acetic acid gradually decreased with increasing reaction time. Meanwhile, a new peak corresponding to C=O stretching vibration of acetyl group appeared at 1630 cm⁻¹ after 10 min and steadily grew up to 15 min [47]. The varying trends of these peaks indicate that CH₃COOH undergoes dehydroxylation to form CH₃CO* over hcp-Co sites. With further increasing time to 20 min, the peak of acetyl gradually disappeared accompanying

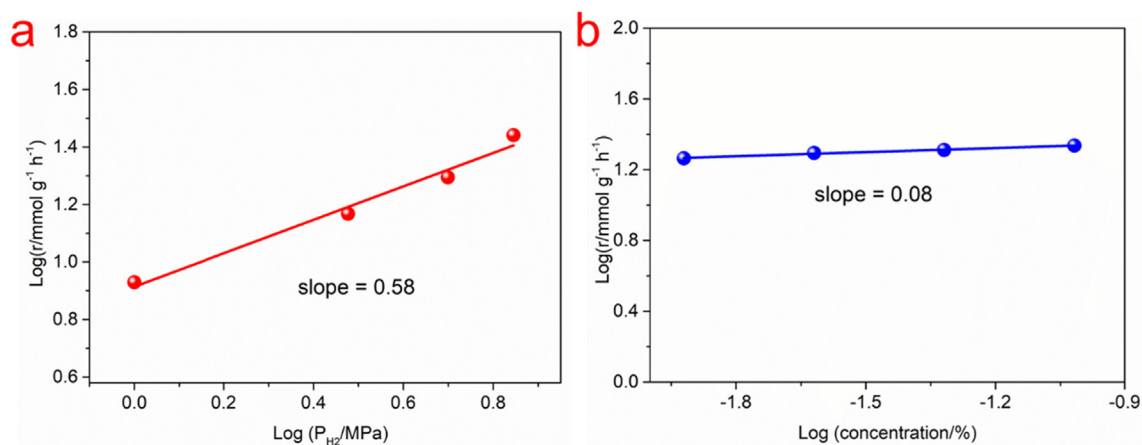


Fig. 6. Effect of (a) H_2 pressure and (b) acetic acid concentration on the reaction rate (r) of acetic acid hydrogenation over hcp-Co@G400. Reaction conditions: 0.05 g catalyst, 220 °C, 2 h.

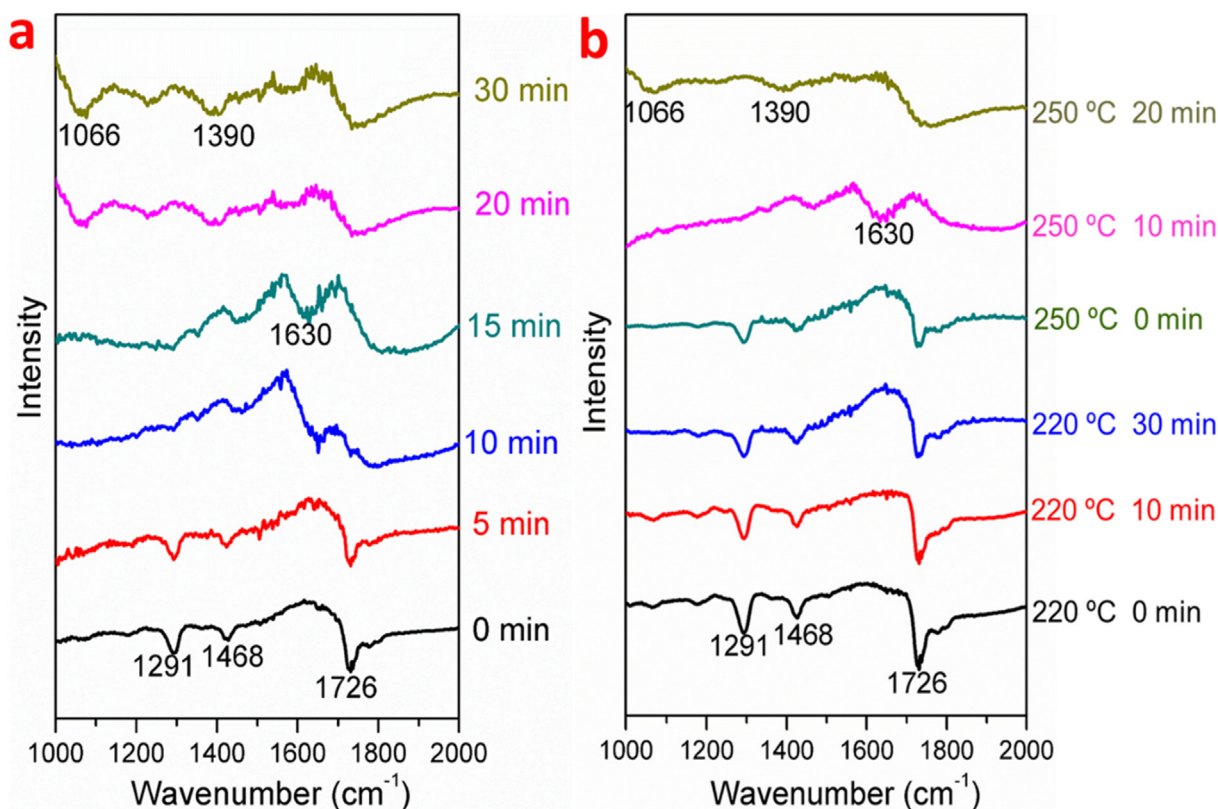


Fig. 7. In situ DRIFTS spectroscopy of acetic hydrogenation over (a) hcp-Co@G400 at 220 °C and (b) 60fcc-Co@G400.

with the presence of ethanol vibration peaks at 1390 (CH_3) and 1066 cm^{-1} (C–O) [45,49]. These evidences confirm that acetic acid hydrogenation to ethanol is proceeded through the acetyl pathway on hcp-Co surface. Although a similar phenomenon was observed for acetic acid hydrogenation over 60fcc-Co@G400 (Fig. 7b), its activity was much lower than that of hcp-Co@G400. No surface reaction occurred at 220 °C and it began to react at 250 °C. The very poor reactivity of 60fcc-Co@G400 is consistent with the evaluation results.

We carried out DFT calculations to investigate the reaction mechanism on hcp-Co and fcc-Co catalysts. The hcp-Co (002) and fcc-Co (111) surfaces were modelled (Fig. S13) based on the

most exposed crystalline facets, as evidenced by XRD and TEM results. The optimized structures and adsorption energies for all the possible species were first calculated and the results are summarized at Fig. 8, Table S3 and Table S4. CH_3COOH preferably adsorbs at Co top site through carbonyl oxygen, in which the C–C bond is vertical to hcp-Co surface. Its adsorption energy is -0.63 eV and Co–O bond length is 2.081 Å, suggesting its strong chemisorption on hcp-Co surface. Contrarily, the preferred adsorption of CH_3COOH on fcc-Co is very weak with an absorption energy of 0.08 eV and long Co–O bond (2.208 Å), in which the C–C bond is parallel to fcc-Co surface. H_2 , ethanol and all the possible intermediate species exhibit similar or minor differences in adsorption

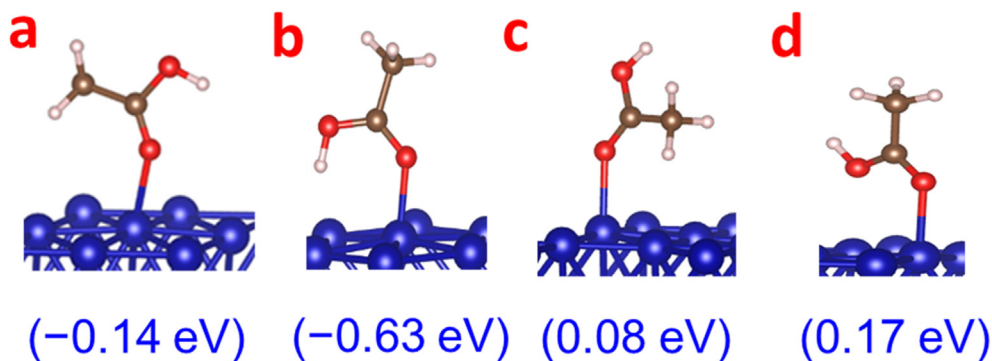


Fig. 8. Adsorption configurations and energies of acetic acid on (a and b) hcp-Co (002) and (c and d) fcc-Co (111) facets. The blue, brown, red and white balls represent Co, C, O and H atoms, respectively. (For interpretation of the references to colour in this figure legend, the reader is referred to the web version of this article.)

configurations and energies on hcp-Co and fcc-Co. H_2 preferentially adsorbs on top sites in hcp-Co, and easily dissociates to H^* on 3-fold hollow sites. The H_2 dissociation (Fig. S14) has nearly no reac-

tion barrier and is thermodynamically favourable process. Moreover, the diffusion of H^* from a hollow site to a nearby hollow site has a very low activation barrier of 0.15 eV, suggesting its high

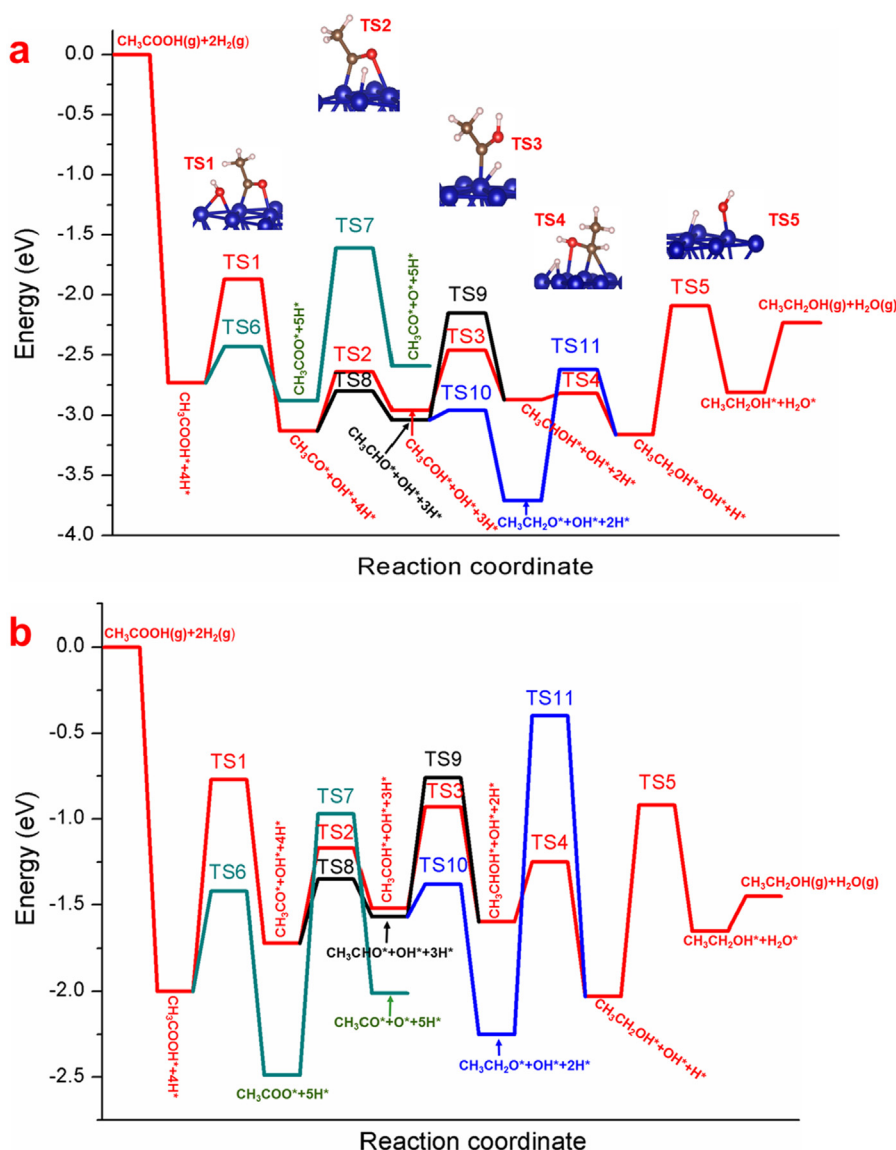


Fig. 9. Potential energy surfaces of acetic acid hydrogenation to ethanol on (a) hcp-Co (002) and (b) fcc-Co (111) surfaces. The blue, brown, red and white balls represent Co, C, O and H atoms, respectively. (For interpretation of the references to colour in this figure legend, the reader is referred to the web version of this article.)

mobility. Similar behaviour is observed on fcc-Co, confirming that metal Co possesses excellent H₂ activation ability, irrespective of crystallite phase.

Based on all the possible elementary reactions, the full potential energy surface of acetic acid hydrogenation over hcp-Co are displayed in Fig. 9a and their transition state (TS) configurations are listed in Table S5. CH₃CO* is the first generated intermediate, no matter the reaction occurs via the direct dehydroxylation pathway or the dehydrogenation-deoxygenation pathway. Compared to direct dehydroxylation pathway, the activation energy of initial CH₃COOH* dehydrogenation reaction is lower, while its consecutive deoxygenation is fairly unfavourable owing to the remarkably high activation barrier up to 1.27 eV. Therefore, the CH₃CO* is most probably formed from CH₃COOH* dehydroxylation with a moderate activation energy of 0.86 eV. The generated CH₃CO* species can proceed to hydrogenation of carbonyl group either by initial C–H bond formation to CH₃CHO* or O–H bond formation to CH₃COH*. With lower activity energy of 0.33 eV, C–H bond formation is preferred over O–H bond formation (0.33 eV vs. 0.49 eV), in line with previous calculation results of the hydrogenation of ketones [50,51]. Subsequently, CH₃CHO* undergoes further hydrogenation either by C–H bond formation or O–H bond formation. The formation of CH₃CH₂O* is kinetically and thermodynamically favourable (E_a = 0.08 eV and E_r = –0.67 eV). However, the hydrogenation of CH₃CH₂O* to CH₃CH₂OH* needs significantly high activation barrier of 1.09 eV, suggesting that this reaction pathway is probably not favourable. The formation of CH₃CHOH* from CH₃CHO* hydrogenation by C–H bond also needs high activation energy of 0.89 eV. Moreover, CH₃CHO species were not detected by DRIFTS spectroscopy, suggesting that CH₃CHO pathway is not favoured at all. Then, we reconsider that the hydrogenation of CH₃CO* to CH₃COH* only has a little higher activation energy (0.49 eV) than that of CH₃CHO* formation (0.33 eV). Further generation of CH₃CHOH* by CH₃COH* hydrogenation is remarkably preferred to CH₃CHO* hydrogenation (0.50 eV vs. 0.89 eV). Moreover, consecutive hydrogenation of CH₃CHOH* to final product CH₃CH₂OH* occurs with nearly no activation barrier (0.05 eV), because this is a thermodynamically favourable elementary reaction (–0.29 eV). Thus, it can be deduced that CH₃COOH hydrogenation to ethanol follows the pathway of CH₃COOH* → CH₃CO* → CH₃COH* → CH₃CHOH* → CH₃CH₂OH*, as supported by the in situ DRIFTS spectra results that the CH₃CHO species were not detected. The produced ethanol can easily desorb from hcp-Co (002) surface with 0.29 eV. Notably, the remaining OH* from CH₃COOH* dehydroxylation will react with nearby H* to produce H₂O with rather high activation barrier (1.07 eV), suggesting that this is the determining-rate step for CH₃COOH hydrogenation over hcp-Co.

Although acetic acid hydrogenation follows the same reaction pathway in both hcp-Co and fcc-Co (Fig. 9b), large differences in the reaction and activation energies are clearly observed. The determining-rate step over fcc-Co becomes the formation of CH₃CO* from CH₃COOH* dehydroxylation with a significantly higher activation barrier of 1.23 eV, which leads to poor reaction activity of fcc-Co. The weak parallel adsorption of CH₃COOH on fcc-Co needs to undergo configuration transformation to vertical motif in the formation of TS1, resulting in higher activation barrier in dehydroxylation reaction. Conversely, the vertical adsorption of CH₃COOH on hcp-Co facilitates the formation of TS1 by elongating C–O bond from 1.36 Å to 2.08 Å, which greatly declines the activation barrier to 0.86 eV. Another elementary reaction of CH₃CHOH + H → CH₃CH₂OH also have moderate difference in activation barrier. For CH₃CHOH* configuration, the C–C tilt angle relative to hcp-Co surface is more similar to that of CH₃CH₂OH* and only a small distortion in the formation of TS4 geometry, thus leading to lower activation energy in comparison to fcc-Co.

4. Conclusions

In this work, we have successfully synthesized pure hcp-Co NPs encapsulated in few-layer graphene via the reduction of Co₂C intermediate from MOF precursor. The graphene shell enables metastable hcp-Co NPs to be strongly confined in the inner space, which can resist not only their allotropic transformation upon high temperature treatment but also their leaching against strong carboxylic acids. Compared to conventional 60fcc-Co@G400, hcp-Co@G400 exhibited one magnitude enhancement in reaction activity of carboxylic acid hydrogenation to alcohol. Moreover, the graphene encapsulated hcp-Co@G400 showed extensive substrate tolerance and excellent reusability. In situ DRIFTS and DFT calculation in model acetic acid hydrogenation reaction reveal that carboxylic acid hydrogenation initially undergoes dehydroxylation to RCO* followed by its consecutive hydrogenation to RCH₂OH. The enhanced reaction reactivity of hcp-Co over fcc-Co is mainly due to the decreasing activation energy from 1.23 eV to 0.86 eV in acetic acid dehydroxylation, which is associated with their distinct CH₃COOH adsorption configurations.

Declaration of Competing Interest

The authors declare that they have no known competing financial interests or personal relationships that could have appeared to influence the work reported in this paper.

Acknowledgements

We are grateful to the financial support from National Natural Science Foundation of China (21878321), Science Foundation for Youth Scholars of State Key Laboratory of Coal Conversion (2016BWZ002), and Youth Innovation Promotion Association CAS (2015140).

Appendix A. Supplementary data

Supplementary data to this article can be found online at <https://doi.org/10.1016/j.jcat.2021.05.013>.

References

- [1] P. Gallezot, Conversion of biomass to selected chemical products, *Chem. Soc. Rev.* 41 (2012) 1538–1558.
- [2] C.-H. Zhou, X. Xia, C.-X. Lin, D.-S. Tong, J. Beltramini, Catalytic conversion of lignocellulosic biomass to fine chemicals and fuels, *Chem. Soc. Rev.* 40 (2011) 5588–5617.
- [3] X. Cui, Y. Li, C. Topf, K. Junge, M. Beller, Direct Ruthenium-catalyzed hydrogenation of carboxylic acids to alcohols, *Angew. Chem. Inter. Ed.* 54 (2015) 10596–10599.
- [4] F.M.A. Geilen, B. Engendahl, M. Hölscher, J. Klankermayer, W. Leitner, Selective homogeneous hydrogenation of biogenic carboxylic acids with [Ru(TriPhos)H]⁺: A mechanistic study, *J. Am. Chem. Soc.* 133 (2011) 14349–14358.
- [5] H. Yim, R. Haselbeck, W. Niu, C. Pujol-Baxley, A. Burgard, J. Boldt, J. Khandurina, J.D. Trawick, R.E. Osterhout, R. Stephen, J. Estadilla, S. Teisan, H.B. Schreyer, S. Andrae, T.H. Yang, S.Y. Lee, M.J. Burk, S. Van Dien, Metabolic engineering of *Escherichia coli* for direct production of 1,4-butanediol, *Nat. Chem. Biol.* 7 (2011) 445.
- [6] Z. Huang, K.J. Barnett, J.P. Chada, Z.J. Brentzel, Z. Xu, J.A. Dumesic, G.W. Huber, Hydrogenation of γ -butyrolactone to 1,4-butanediol over CuCo/TiO₂ bimetallic catalysts, *ACS Catal.* 7 (2017) 8429–8440.
- [7] T.P. Brewster, A.J.M. Miller, D.M. Heinekey, K.I. Goldberg, Hydrogenation of carboxylic acids catalyzed by half-sandwich complexes of iridium and rhodium, *J. Am. Chem. Soc.* 135 (2013) 16022–16025.
- [8] J. Pritchard, G.A. Filonenko, R. van Putten, E.J.M. Hensen, E.A. Pidko, Heterogeneous and homogeneous catalysis for the hydrogenation of carboxylic acid derivatives: history, advances and future directions, *Chem. Soc. Rev.* 44 (2015) 3808–3833.
- [9] J. Ullrich, B. Breit, Selective hydrogenation of carboxylic acids to alcohols or alkanes employing a heterogeneous catalyst, *ACS Catal.* 8 (2018) 785–789.

- [10] Y. Takeda, T. Shoji, H. Watanabe, M. Tamura, Y. Nakagawa, K. Okumura, K. Tomishige, Selective hydrogenation of lactic acid to 1,2-propanediol over highly active ruthenium–molybdenum oxide catalysts, *ChemSusChem* 8 (2015) 1170–1178.
- [11] H.G. Manyar, C. Paun, R. Pilus, D.W. Rooney, J.M. Thompson, C. Hardacre, Highly selective and efficient hydrogenation of carboxylic acids to alcohols using titania supported Pt catalysts, *Chem. Commun.* 46 (2010) 6279–6281.
- [12] Y. Takeda, M. Tamura, Y. Nakagawa, K. Okumura, K. Tomishige, Hydrogenation of dicarboxylic acids to diols over Re–Pd catalysts, *Catal. Sci. Technol.* 6 (2016) 5668–5683.
- [13] T.J. Korstanje, J. Ivar van der Vlugt, C.J. Elsevier, B. de Bruin, Hydrogenation of carboxylic acids with a homogeneous cobalt catalyst, *Science* 350 (2015) 298–302.
- [14] H. Bin Wu, X.W. Lou, Metal-organic frameworks and their derived materials for electrochemical energy storage and conversion: Promises and challenges, *Sci. Adv.* 3 (2017) 9252.
- [15] L. Fan, P.F. Liu, X. Yan, L. Gu, Z.Z. Yang, H.G. Yang, S. Qiu, X. Yao, Atomically isolated nickel species anchored on graphitized carbon for efficient hydrogen evolution electrocatalysis, *Nat. Commun.* 7 (2016) 10667.
- [16] B.Y. Xia, Y. Yan, N. Li, H.B. Wu, X.W. Lou, X. Wang, A metal-organic framework-derived bifunctional oxygen electrocatalyst, *Nat. Energy* 1 (2016) 15006.
- [17] J. Deng, P. Ren, D. Deng, X. Bao, Enhanced electron penetration through an ultrathin graphene layer for highly efficient catalysis of the hydrogen evolution reaction, *Angew. Chem. Inter. Ed.* 54 (2015) 2100–2104.
- [18] K.M. Rajenahally, V. Jagadeesh, A.S. Alshammari, H. Neumann, M.-M. Pohl, J. Radnik, 1 Matthias Beller, MOF-derived cobalt nanoparticles catalyze a general synthesis of amines, *Science* 358 (2017) 326–332.
- [19] V.P. Santos, T.A. Wezendonk, J.J.D. Jaén, A.I. Dugulan, M.A. Nasalevich, H.-U. Islam, A. Chojacki, S. Sartipi, X. Sun, A.A. Hakeem, A.C.J. Koeken, M. Ruitenbeek, T. Davidian, G.R. Meima, G. Sankar, F. Kapteijn, M. Makkee, J. Gascon, Metal organic framework-mediated synthesis of highly active and stable Fischer-Tropsch catalysts, *Nat. Commun.* 6 (2015) 6451.
- [20] J. Tang, R.R. Salunkhe, J. Liu, N.L. Torad, M. Imura, S. Furukawa, Y. Yamauchi, Thermal conversion of core-shell metal-organic frameworks: A new method for selectively functionalized nanoporous hybrid carbon, *J. Am. Chem. Soc.* 137 (2015) 1572–1580.
- [21] X. Ma, Y.-X. Zhou, H. Liu, Y. Li, H.-L. Jiang, A MOF-derived Co–CoO@N-doped porous carbon for efficient tandem catalysis: Dehydrogenation of ammonia borane and hydrogenation of nitro compounds, *Chem. Commun.* 52 (2016) 7719–7722.
- [22] L. Yu, J.F. Yang, X.W. Lou, Formation of CoS₂ nanobubble hollow prisms for highly reversible lithium storage, *Angew. Chem. Inter. Ed.* 55 (2016) 13422–13426.
- [23] H. Hu, B. Guan, B. Xia, X.W. Lou, Designed formation of Co₃O₄/NiCo₂O₄ double-shelled nanocages with enhanced pseudocapacitive and electrocatalytic properties, *J. Am. Chem. Soc.* 137 (2015) 5590–5595.
- [24] W.-Z. Li, J.-X. Liu, J. Gu, W. Zhou, S.-Y. Yao, R. Si, Y. Guo, H.-Y. Su, C.-H. Yan, W.-X. Li, Y.-W. Zhang, D. Ma, Chemical insights into the design and development of face-centered cubic ruthenium catalysts for Fischer-Tropsch synthesis, *J. Am. Chem. Soc.* 139 (2017) 2267–2276.
- [25] J.-X. Liu, H.-Y. Su, D.-P. Sun, B.-Y. Zhang, W.-X. Li, Crystallographic dependence of CO activation on cobalt catalysts: HCP versus FCC, *J. Am. Chem. Soc.* 135 (2013) 16284–16287.
- [26] S. Lyu, L. Wang, J. Zhang, C. Liu, J. Sun, B. Peng, Y. Wang, K.G. Rappé, Y. Zhang, J. Li, L. Nie, Role of active phase in Fischer-Tropsch synthesis: Experimental evidence of CO activation over single-phase cobalt catalysts, *ACS Catal.* 8 (2018) 7787–7798.
- [27] Y.-P. Pei, J.-X. Liu, Y.-H. Zhao, Y.-J. Ding, T. Liu, W.-D. Dong, H.-J. Zhu, H.-Y. Su, L. Yan, J.-L. Li, W.-X. Li, High alcohols synthesis via Fischer-Tropsch reaction at cobalt metal/carbide interface, *ACS Catal.* 5 (2015) 3620–3624.
- [28] R.W. Mitchell, D.C. Lloyd, L.G.A. van de Water, P.R. Ellis, K.A. Metcalfe, C. Sibbald, L.H. Davies, D.I. Enache, G.J. Kelly, E.D. Boyes, P.L. Gai, Effect of pretreatment method on the nanostructure and performance of supported Co catalysts in Fischer-Tropsch synthesis, *ACS Catal.* 8 (2018) 8816–8829.
- [29] M. Sadeqzadeh, H. Karaca, O.V. Safonova, P. Fongarland, S. Chambrey, P. Roussel, A. Griboval-Constant, M. Lacroix, D. Curulla-Ferré, F. Luck, A.Y. Khodakov, Identification of the active species in the working alumina-supported cobalt catalyst under various conditions of Fischer-Tropsch synthesis, *Catal. Today* 164 (2011) 62–67.
- [30] A.n. Martínez, C. López, F. Márquez, I. Díaz, Fischer-Tropsch synthesis of hydrocarbons over mesoporous Co/SBA-15 catalysts: the influence of metal loading, cobalt precursor, and promoters, *J. Catal.* 220 (2003) 486–499.
- [31] G. Kresse, D. Joubert, From ultrasoft pseudopotentials to the projector augmented-wave method, *Phys. Rev. B* 59 (1999) 1758–1775.
- [32] J.P. Perdew, K. Burke, M. Ernzerhof, Generalized gradient approximation made simple, *Phys. Rev. Lett.* 77 (1996) 3865–3868.
- [33] G. Henkelman, B.P. Uberuaga, H. Jónsson, A climbing image nudged elastic band method for finding saddle points and minimum energy paths, *J. Chem. Phys.* 113 (2000) 9901–9904.
- [34] L. Han, X.-Y. Yu, X.W. Lou, Formation of prussian-blue-analog nanocages via a direct etching method and their conversion into Ni–Co-mixed oxide for enhanced oxygen evolution, *Adv. Mater.* 28 (2016) 4601–4605.
- [35] Y. Yang, Z. Lin, S. Gao, J. Su, Z. Lun, G. Xia, J. Chen, R. Zhang, Q. Chen, Tuning electronic structures of nonprecious ternary alloys encapsulated in graphene layers for optimizing overall water splitting activity, *ACS Catal.* 7 (2017) 469–479.
- [36] V.A. de la Peña O’Shea, P.R. de la Piscina, N. Homs, G. Aromí, J.L.G. Fierro, Development of hexagonal closed-packed cobalt nanoparticles stable at high temperature, *Chem. Mater.* 21 (2009) 5637–5643.
- [37] N. Osakoo, R. Henkel, S. Loiha, F. Roessner, J. Wittayakun, Palladium-promoted cobalt catalysts supported on silica prepared by impregnation and reverse micelle for Fischer-Tropsch synthesis, *Appl. Catal. A: Gen.* 464–465 (2013) 269–280.
- [38] Z. Zhao, W. Lu, R. Yang, H. Zhu, W. Dong, F. Sun, Z. Jiang, Y. Lyu, T. Liu, H. Du, Y. Ding, Insight into the formation of Co@Co₂C catalysts for direct synthesis of higher alcohols and olefins from syngas, *ACS Catal.* 8 (2018) 228–241.
- [39] H. Fei, J. Dong, Y. Feng, C.S. Allen, C. Wan, B. Voloskiy, M. Li, Z. Zhao, Y. Wang, H. Sun, P. An, W. Chen, Z. Guo, C. Lee, D. Chen, I. Shakir, M. Liu, T. Hu, Y. Li, A.I. Kirkland, X. Duan, Y. Huang, General synthesis and definitive structural identification of MN₄C₄ single-atom catalysts with tunable electrocatalytic activities, *Nat. Catal.* 1 (2018) 63–72.
- [40] W. Luo, M. Sankar, A.M. Beale, Q. He, C.J. Kiely, P.C.A. Bruijninx, B.M. Weckhuysen, High performing and stable supported nano-alloys for the catalytic hydrogenation of levulinic acid to γ -valerolactone, *Nat. Commun.* 6 (2015) 6540.
- [41] D.J.M. de Vlieger, L. Lefferts, K. Seshan, Ru decorated carbon nanotubes – a promising catalyst for reforming bio-based acetic acid in the aqueous phase, *Green Chem.* 16 (2014) 864–874.
- [42] T. Toyao, S.M. Siddiki, A.S. Touchy, W. Onodera, K. Kon, Y. Morita, T. Kamachi, K. Yoshizawa, K. Shimizu, TiO₂-supported Re as a general and chemoselective heterogeneous catalyst for hydrogenation of carboxylic acids to alcohols, *Chem. Eur. J.* 23 (2017) 1001–1006.
- [43] H. Olcay, L. Xu, Y. Xu, G.W. Huber, Aqueous-phase hydrogenation of acetic acid over transition metal catalysts, *ChemCatChem* 2 (2010) 1420–1424.
- [44] V. Pallassana, M. Neurock, Reaction paths in the hydrogenolysis of acetic acid to ethanol over Pd (111), Re (0001), and PdRe alloys, *J. Catal.* 209 (2002) 289–305.
- [45] W. Rachmady, M.A. Vannice, Acetic acid reduction by H₂ over supported Pt catalysts: A DRIFTS and TPD/TPR study, *J. Catal.* 207 (2002) 317–330.
- [46] M. Zhang, R. Yao, H. Jiang, G. Li, Y. Chen, Insights into the mechanism of acetic acid hydrogenation to ethanol on Cu (111) surface, *Appl. Surf. Sci.* 412 (2017) 342–349.
- [47] L. Chen, Y. Zhu, H. Zheng, C. Zhang, Y. Li, Aqueous-phase hydrodeoxygenation of propanoic acid over the Ru/ZrO₂ and Ru–Mo/ZrO₂ catalysts, *Appl. Catal. A: Gen.* 411–412 (2012) 95–104.
- [48] L. Chen, Y. Zhu, H. Zheng, C. Zhang, B. Zhang, Y. Li, Aqueous-phase hydrodeoxygenation of carboxylic acids to alcohols or alkanes over supported Ru catalysts, *J. Mol. Catal. A: Chem.* 351 (2011) 217–227.
- [49] M. Tamura, R. Tamura, Y. Takeda, Y. Nakagawa, K. Tomishige, Insight into the mechanism of hydrogenation of amino acids to amino alcohols catalyzed by a heterogeneous MoO_x-modified Rh catalyst, *Chem. Eur. J.* 21 (2015) 3097–3107.
- [50] O. Mamun, E. Walker, M. Faheem, J.Q. Bond, A. Heyden, Theoretical investigation of the hydrodeoxygenation of levulinic acid to γ -valerolactone over Ru (0001), *ACS Catal.* 7 (2017) 215–228.
- [51] O. Mamun, M. Saleheen, J.Q. Bond, A. Heyden, Importance of angelica lactone formation in the hydrodeoxygenation of levulinic acid to γ -valerolactone over a Ru (0001) model surface, *J. Phys. Chem. C* 121 (2017) 18746–18761.